Biogeosciences Discuss., 12, 3905–3942, 2015
www.biogeosciences-discuss.net/12/3905/2015/
doi:10.5194/bgd-12-3905-2015

Biogeosciences Discussions
Open Access

A new parameterization for surface ocean light attenuation in Earth System Models: assessing the impact of light absorption by colored detrital material

G. E. Kim, M.-A. Pradal, and A. Gnanadesikan

Department of Earth and Planetary Sciences, 301 Olin Hall, 3400 N. Charles Street, Baltimore, MD 21218, USA

Received: 17 December 2014 – Accepted: 27 January 2015 – Published: 2 March 2015

Correspondence to: G. E. Kim (gracekim@jhu.edu)

Published by Copernicus Publications on behalf of the European Geosciences Union.

Abstract

Light limitation can affect the distribution of biota and nutrients in the ocean. Light absorption by colored detrital material (CDM) was included in a fully coupled Earth System Model using a new parameterization for shortwave attenuation. Two model runs were conducted, with and without light attenuation by CDM. In a global average sense, greater light limitation associated with CDM increased surface chlorophyll, biomass and nutrients together. These changes can be attributed to the movement of biological productivity higher up the water column, which increased surface chlorophyll and biomass while simultaneously decreasing total biomass. Meanwhile, the reduction in biomass resulted in greater nutrient availability throughout the water column. Similar results were found on a regional scale in an analysis of the oceans by biome. In coastal regions, surface chlorophyll increased by 35 % while total integrated phytoplankton biomass diminished by 18 %. The largest relative increases in modeled surface chlorophyll and biomass in the open ocean were found in the equatorial biomes, while largest decreases in depth-integrated biomass and chlorophyll were found in the subpolar and polar biomes. This mismatch of surface and subsurface trends and their regional dependence was analyzed by comparing the competing factors of diminished light availability and increased nutrient availability on phytoplankton growth in the upper 200 m. Overall, increases in surface biomass were expected to accompany greater nutrient uptake and therefore diminish surface nutrients, but changes in light limitation decoupled trends between these two variables. Understanding changes in biological productivity requires both surface and depth-resolved information. Surface trends may be minimal or of the opposite sign to depth-integrated amounts, depending on the vertical structure of phytoplankton abundance.

BGD
12, 3905–3942, 2015

1 Introduction

The attenuation of shortwave solar radiation in the surface ocean exerts a primary control on ocean biology, since light is necessary for photosynthesis by phytoplankton. The decay of incident surface irradiance $I_d(0,\lambda)$ with increasing depth z in the water column can be approximated as an exponential function:

$$I_d(z,\lambda) = I_d(0,\lambda)\exp\left(-\int_0^z k_d(z',\lambda)\mathrm{d}z'\right), \quad (1)$$

where k_d (units of m^{-1}) is the spectral attenuation coefficient for downwelling irradiance. The reciprocal of k_d is the first e-folding depth of the incident light on the surface of the ocean, an intuitive length scale for the well-lit surface ocean. Variations in shortwave attenuation have been related to measured quantities of constituents in the aquatic medium, such as concentrations of the phytoplankton pigment concentration chlorophyll *a*. Morel (1988) observed increasing k_d with increasing chlorophyll *a* pigment concentration in 176 concurrent in situ measurements, excluding stations where light attenuation was dominated by "yellow substance" or turbidity. These measurements were used to develop a function that relates k_d to chlorophyll *a* concentration of the form:

$$k_d(\lambda) = k_w(\lambda) + \chi(\lambda)[\mathrm{chl}]^{e(\lambda)}, \quad (2)$$

where $k_w(\lambda)$ is the attenuation by pure seawater, [chl] is the chlorophyll *a* concentration and $\chi(\lambda)$ and $e(\lambda)$ are the wavelength-dependent coefficient and exponent. This parameterization implicitly includes the light attenuation of all other aquatic constituents directly in proportion to chlorophyll concentration. Ohlmann and Siegel (2000) used a radiative transfer numerical model to develop an extended parameterization for k_d which depended on chlorophyll concentration, cloudiness and solar zenith angle to include the effects of varying physical conditions over ocean waters. Among these four

BGD
12, 3905–3942, 2015

variables, chlorophyll concentration was found to have the largest influence on reducing solar transmission below 1 m.

These initial parameterizations have been adapted for use in Ocean General Circulation Models (OGCMs) and Earth System Models (ESMs) to study the influence of spatially varying light attenuation associated with varying concentrations of phytoplankton pigments in the ocean. Although numerous model experiments of this type were conducted, we mostly limit our introductory material to studies that utilized versions of the parameterization shown in Eq. (2). These studies examined the effects of applying a spatially varying k_d calculated from annual mean chlorophyll data, estimated by ocean color satellites, compared to the base case of a constant attenuation depth. Murtugudde et al. (2002) employed the Morel parameterization (Eq. 2) spectrally averaged over visible wavelengths, from 400 to 700 nm, to calculate k_d(vis) with chlorophyll *a* concentration estimates from the ocean color satellite Coastal Zone Color Scanner (CZCS). Spatially varying the attenuation depth improved the OGCM SST simulation in the Pacific cold tongue and during ENSO events and in the Atlantic near river outflows. Subsequent studies employed an optics model that separately attenuated visible light in two bands of equal energy, nominally the "blue-green", k_d(bg), and "red" bands, $k_d(r)$, as specified in (Manizza et al., 2005):

$$k_d(\mathrm{bg}) = 0.0232 + 0.074 \cdot [\mathrm{chl}]^{0.674} \quad (3)$$

$$k_d(r) = 0.225 + 0.037 \cdot [\mathrm{chl}]^{0.629}. \quad (4)$$

Studies that applied this k_d parameterization in fully coupled ESMs were uniquely able to assess how changes in oceanic shortwave absorption can affect atmospheric circulation via changes in SST. Gnanadesikan and Anderson (2009) observed changes in strength of the Hadley and Walker circulations when applying a spatially-varying k_d using chlorophyll concentration from the SeaWiFS (Sea-viewing Wide Field-of-view Sensor) ocean color satellite relative to a clear ocean with no chlorophyll. Alternatively, Manizza et al. (2005) applied this parameterization to an OGCM with a biogeochemical model to calculate k_d using modeled chlorophyll concentration instead of surface

BGD
12, 3905–3942, 2015

chlorophyll estimates from satellite. The main advantage of the latter model configuration is that phytoplankton can respond to changes in environmental variables. They found that adding phytoplankton amplified the seasonal cycles of SST, mixed layer depth and sea-ice cover, which in turn created environmental conditions that were favorable to additional phytoplankton growth.

Although variations in light attenuation in ESMs were previously attributed to phytoplankton pigment only, other optically significant aquatic constituents can now be incorporated into models. This paper is concerned with the omission of colored detrital material (CDM) in approximations of light decay in the current generation of ESMs. CDM consists of chromophoric dissolved organic matter (CDOM) and non-algal detrital particles (NAP). It is operationally defined by its spectrally-dependent absorption coefficient of light, a_{dg} (units of m^{-1}), which represents the fraction of incident power that is absorbed by detrital matter in a water sample over a given pathlength. The absorption coefficient is given the subscript "dg" to represent the sum of the two component absorption coefficients; (1) non-algal detrital particles, a_{NAP}, and (2) light-absorbing dissolved organic matter which passes through a 0.2–0.4 µm filter, a_{CDOM}, (called *gelbstoff* by early researchers in optical oceanography, hence the "g" in "dg"): $a_{dg} = a_{NAP} + a_{CDOM}$. Measurements suggest CDOM accounts for a large fraction of non-water absorption in the open ocean, especially in the UV and blue wavelengths (Siegel et al., 2005; Nelson and Siegel, 2013). The attenuation of light by this strongly absorbing component should be included in Earth System Models. Although light absorption by NAP is a small fraction of CDM absorption (see Fig. 1), the sum of NAP and CDOM is considered because existing satellite algorithms cannot separate the contribution of each component.

Moreover, parameterizing k_d using Eq. (2) relies on the validity of the bio-optical assumption, which states that all light-attenuating constituents covary with chlorophyll concentration. Yet processes that influence CDM abundance, such as freshwater delivery of terrestrial organic matter and photobleaching, can behave independently of chlorophyll *a* concentration, rendering the bio-optical assumption inappropriate for

BGD
12, 3905–3942, 2015

some aquatic environments. In this paper, we will consider the impact of decoupling the optical influence of chlorophyll *a* and CDM in Earth System Models. Gregg and Casey (2009) previously developed a more optically complex model for surface ocean irradiance based on light absorption and scattering of aquatic constituents. However, this study was primarily concerned with accurately modeling surface irradiance and photosynthetically available radiation for comparison with in situ and satellite data. The current paper is concerned with using an Earth System model to better understand how changes in light will affect ocean ecosystems.

In Sect. 2, we introduce the global ocean color dataset for the absorption coefficient of detritus and CDOM, and discuss its incorporation into the GFDL CM2Mc ESM with BLING biogeochemistry model. This is accomplished using a newly developed parameterization for $k_d(\lambda)$, which aims to represent light attenuation by chlorophyll *a* and CDM as independently varying phenomena. (For the remainder of this paper, we will refer to chlorophyll *a* concentration simply as chlorophyll.) Section 3 details the model runs and the results, with a focus on how changes in light affect chlorophyll, biomass and nutrient concentrations. The paper concludes with Sect. 4, discussing the implications of our findings and suggestions for future work.

2 Methodology

2.1 Light penetration parameterization

A new k_d parameterization was developed for implementation in the GFDL CM2Mc ESM (Galbraith et al., 2011) with BLING ocean biogeochemistry (Galbraith et al., 2010). In its current configuration, the CM2Mc-BLING system uses the Manizza et al. (2005) optics model and k_d parameterization as shown in Eqs. (3) and (4). The new parameterization was developed from this optics model, revising the k_d(bg) parameterization only (Eq. 3). The $k_d(r)$ parameterization was unchanged because light absorption by CDOM in red wavelengths is much smaller than in the blue-green wavelengths

BGD
12, 3905–3942, 2015

which can be seen from the spectral shape of a_{dg} in Fig. 1. The new k_d(bg) parameterization incorporates the absorption coefficient of detritus and CDOM at wavelength 443 nm, a_{dg}(443), because field measurements of a_{dg} are available at this wavelength. In addition, existing satellite data products of a_{dg} are readily available for this wavelength only.

In the new parameterization, the dependence of k_d(bg) on both chlorophyll concentration and a_{dg}(443) is the best fit function between concurrent in situ measurements of these variables from the NASA bio-Optical Marine Algorithm Dataset (NOMAD) (Werdell and Bailey, 2005). Measurements of k_d from 400 to 530 nm were energy-weighted and averaged to get a single value for the attenuation coefficient in the blue-green wavelengths. There were 244 concurrent measurements of k_d(bg), chlorophyll concentration and a_{dg}(443) from the NOMAD dataset, representing both coastal and open ocean waters. The best fit surface for these three variables was found using a least-squares polynomial regression model, resulting in the following parameterization:

$$k_d(\mathrm{bg}) = 0.0232 + 0.0513 \cdot [\mathrm{chl}]^{0.668} + 0.710 \cdot a_{dg}(443)^{1.13}. \quad (5)$$

Equation (5) is qualitatively different from the previous parameterization, Eq. (3), in several ways. The attenuation coefficient is less dependent on chlorophyll concentration, with a smaller coefficient and exponent on the chlorophyll term in Eq. (5) compared to Eq. (3). Meanwhile, the additional a_{dg}(443) term makes the water more opaque in locations where CDM and chlorophyll concentration are not well correlated, such as coastal zones that are strongly influenced by the terrestrial delivery of CDOM. The k_d dependence on a_{dg}(443) is superlinear, which at first glance seems to suggest an unexpectedly strong dependence on CDOM and detrital particles. We suggest this superlinear relationship is justified because the parameterization is fitting for spatial variations in CDOM quality and quantity. Measurements of the a_{dg} across the ultraviolet to visible spectrum suggest the spectral dependence of light absorption by CDOM is regionally specific (Nelson and Siegel, 2013).

BGD
12, 3905–3942, 2015

2.2 Implementation in ESM

This parameterization was implemented in the GFDL CM2Mc ESM, a coarse resolution coupled global climate model with land, ice, atmosphere and ocean components (Galbraith et al., 2011). The Modular Ocean Model version 4p1 code is used to simulate the ocean. The model has a varying horizontal resolution from 0.6 to 3° and 28 vertical levels of increasing thickness with depth. Ocean biogeochemistry is represented by the Biogeochemistry with Light, Iron, Nutrients and Gases model (BLING), which is embedded in the ocean component of the physical model (Galbraith et al., 2010). The coupling between the biogeochemical model and physical model allows changes in chlorophyll concentration to produce changes in shortwave radiation absorption and vice versa.

In the BLING biogeochemical model, phytoplankton growth rate is calculated implicitly as a function of temperature, macronutrient concentration, iron concentration and light.

$$\mu = P_0^C \times \exp(kT) \times \text{nlim} \times \text{llim} \tag{6}$$

where μ is a carbon-specific growth rate, P_0^C is a maximum growth rate at 0 °C, $\exp(kT)$ is a temperature-dependent term based on Eppley (1972), $\text{nlim} = \min(\text{Fe}_D, \frac{PO_4}{k_{PO_4}+PO_4})$ is a nutrient limitation term following a Liebig's law of the minimum and $\text{llim} = (1 - \exp(\frac{-I}{I_k}))$ is a light limitation term. These nutrient and light limitation factors, nlim and llim, represent the extent to which the optimal photosynthetic growth rate is scaled down by nutrient and light availability. Furthermore, these are the only two variables that determine biomass in the BLING model. Total biomass is a sum of large and small phytoplankton groups, which are related to growth rate μ by the following equation

$$B = B_{\text{large}} + B_{\text{small}} = P^* \left(\left(\frac{\mu}{\lambda}\right)^3 + \left(\frac{\mu}{\lambda}\right) \right) \tag{7}$$

BGD
12, 3905–3942, 2015

where B is biomass, P^* is a scale factor for phytoplankton concentration and λ is a temperature-dependent mortality rate

$$\lambda = \lambda_0 \times \exp(kT). \tag{8}$$

Substituting Eqs. (6) and (8) for μ and λ into Eq. (7), gives us

$$B = P^* \left(\left(\frac{P_0^C \times \exp(kT) \times \text{nlim} \times \text{llim}}{\lambda_0 \times \exp(kT)} \right)^3 + \left(\frac{P_0^C \times \exp(kT) \times \text{nlim} \times \text{llim}}{\lambda_0 \times \exp(kT)} \right) \right) \tag{9}$$

Following Dunne et al. (2005), the temperature dependence of the mortality rate is set identical to that of the growth rate such that the $\exp(kT)$ term in both μ and λ expressions are identical, Eq. (9) reduces to the following relationship between biomass, nutrient limitation and light limitation

$$B \propto (C(\text{nlim} \times \text{llim})^3 + (\text{nlim} \times \text{llim})). \tag{10}$$

Dunne et al. (2005) found that such a formulation was able to reproduce the observed phytoplankton size structure in 40 samples. This allows us to separately evaluate the contributions of nutrient and light limitation to changes in biomass in our biogeochemical model. This relationship will be utilized in the Results section of our paper.

Chlorophyll concentration is calculated from biomass using a varying chl : C ratio to account for photoadaptation. Large scale patterns and features of chlorophyll concentration are qualitatively represented, with lower chlorophyll concentration in the gyres and higher concentrations in mid- to high-northern latitudes and equatorial upwelling zones (see Fig. 3). In general, the annual average modeled chlorophyll exceeds the satellite observed chlorophyll concentration in the open ocean. The seasonal cycle is also well-represented, but with a northern latitude spring bloom onset earlier than appears in satellite data. There is good spatial agreement between the modeled and observed spatial distribution of macronutrient, which is shown in Fig. 4. BLING only

BGD
12, 3905–3942, 2015

models phosphate concentration, which is comparable to an "average macronutrient" that represents the average concentrations of phosphate and nitrate scaled to phosphate by the N : P Redfield ratio, $\frac{1}{2}(PO_4 + \frac{NO_3}{16})$ (Galbraith et al., 2010). The error in chlorophyll and nutrient concentrations in this implementation of BLING are worse than in Galbraith et al. (2010) because the model parameters were originally tuned to a data-driven ocean model. As a result, errors that appear in the physical circulation will also appear in the biological solution.

The ocean optical model receives incoming shortwave radiation from the atmospheric component. Visible light is divided and then averaged into two spectral bands, blue-green and red, which is then attenuated by k_d(bg) and $k_d(r)$ respectively. In its previous configuration, BLING calculated k_d(bg) as a function of chlorophyll concentration as shown in Eq. (3). For this study, k_d(bg) is calculated using Eq. (5) with model-predicted chlorophyll concentration and fixed $a_{dg}(443)$ from satellite climatology. The $a_{dg}(443)$ dataset used in this study is the average of the 2002 to 2013 Aqua MODIS GSM $a_{dg}(443)$ Level 3 annual composites from http://oceancolor.gsfc.nasa.gov. Consequently the seasonal variability of CDM is not represented in our model runs. The data was re-gridded to the ocean model's spatial resolution and missing values were filled in by equal weight averaging over the pixel's 8 neighbors using Ferret, a data visualization and analysis tool for gridded datasets (see Fig. 5). Annual average data was used instead of monthly data to maximize the number of grid cells with unimpeded satellite observations. Satellite-estimated values of surface $a_{dg}(443)$ were held constant with increasing depth.

3 Model runs: setup, results and discussion

3.1 Model setup

The GFDL CM2Mc ESM with BLING ocean biogeochemistry was spun up for 1500 years with the Manizza et al. (2005) ocean optics model, allowing dynamical

BGD
12, 3905–3942, 2015

processes to reach equilibrium. New model runs were initialized from this spun up state and were completed for an additional 300 years. The data analyzed in this section are average results from the final 100 years of the two model runs: the (1) "chl&CDM" run utilizes the full k_d(bg) parameterization, Eq. (5), while the (2) "chl-only" run calculates light attenuation with the chlorophyll-dependent term only: $k_d(\mathrm{bg}) = 0.0232 + 0.0513 \cdot [\mathrm{chl}]^{0.668}$. The difference between these (chl&CDM minus chl-only) shows the impact of added shortwave attenuation by CDM. For the remainder of this paper we will refer to k_d(bg) as k_d for simplicity.

3.2 Model results: global trends

Adding CDM to the k_d parameterization shoaled the attenuation depth (k_d^{-1}, in m) in most places. This change in the light field was accompanied by a globally integrated 10 % increase in surface macronutrients, 11 % increase in surface biomass and 16 % increase in surface chlorophyll. These changes reflect the total integrated value from the surface grid box, which represents the uppermost 10 m. At first glance, this result was puzzling since increases in chlorophyll and biomass are generally associated with increased nutrient consumption, which is usually indicated by decreased nutrient concentration. Instead, all three variables increased together. The spatial distributions of surface changes in macronutrients, chlorophyll concentration and biomass are shown in Fig. 6.

In order to understand these surface changes, it is necessary to evaluate changes in the biomass depth profile. Globally averaged biomass and particulate organic carbon (POC) export flux in the chl&CDM run are higher near the surface but diminished at depth, as shown in Fig. 7. Biological productivity moves up in the water column, which explains the increase in surface chlorophyll. Below 25 m, there is less biological productivity in the chl&CDM run. The depth-integrated result is a 9 % decrease in total biomass. Furthermore, since biological productivity is occurring closer to the surface, particulate matter is consumed in the water column and less is exported into the deep

BGD
12, 3905–3942, 2015

ocean. This can be seen in Fig. 7b. The cumulative effect is a 7 % decrease in POC flux at 200 m.

This upward shift in the vertical distribution of biomass was accompanied by increased macronutrients at all depths. Here, we will consider the distribution of macronutrients in the top 200 m as a measure of the biological activity in the mixed layer according to the biological pump efficiency, E_{bp}, defined in Sarmiento and Gruber (2006) as: $E_{bp} = \frac{C_{deep} - C_{surface}}{C_{deep}}$. This metric provides a indication of the extent to which phytoplankton are able to draw down nutrients delivered to the surface from the deep ocean. Here, $C_{surface}$ is the integrated nutrient concentration between 0 and 100 m and C_{deep} is the integrated nutrient concentration between 100 and 200 m. The difference in E_{bp} between the two model runs shows a widespread decrease in biological pump efficiency when CDM is included (see Fig. 8). In a global average sense, increased light limitation by CDM diminishes total biomass, leaving excess nutrients in the water column. Nutrients are more abundant and phytoplankton are less effective at utilizing them when the ocean is more light limited. The spatial correlation between the difference in E_{bp} and a_{dg} is −0.26, indicating a general negative relationship between the two variables. However, regions of greatest light absorption by CDM are not always the same regions of greatest decrease in E_{bp} for reasons that will be discussed in the following subsections.

3.3 Coastal regions

The distribution of light absorption by CDM in Fig. 5 and diminished attenuation depth in Fig. 6 suggest the addition of CDM to the optical model would have a significant impact on ocean productivity in coastal regions. For the following analysis, coastal regions were defined as grid cells adjacent to land.

In coastal regions, surface nutrients increased by 16 %, surface biomass by 22 % and surface chlorophyll by 35 %. Depth-integrated trends were of the opposite sign compared to surface trends. Total biomass decreased by 18 % and total chlorophyll

BGD
12, 3905–3942, 2015

decreased by 17 % when CDM was included. The largest percentage changes in integrated biomass were found in the equatorial latitudes, which experienced up to 38 % drops in coastal biomass. High northern latitudes north of 60° N experienced 17–36 % decreases in coastal biomass. Relative changes in depth-integrated coastal biomass are shown by latitude in Fig. 10.

These results are reported with the understanding that the coastal circulation is likely to be poorly resolved in our coarse model. Nonetheless, they highlight the potential impact of including the optical impact of CDM in coastal regions. The results shown in this paper compare the "chl&CDM" and "chl-only" model runs. A comparison of the output of the "chl&CDM" model run and a model run with the original k_d parameterization, Eq. (3), show similar trends. In coastal regions, surface nutrients increased by 1 %, surface biomass by 3 % and surface chlorophyll by 6 %, while depth-integrated biomass and chlorophyll decreased by 9 % compared to the "chl&CDM" model run. It will be increasingly important for models to include the optical impact of CDM to avoid the potential error of misrepresenting light attenuation as models with finer grid resolution are developed, especially in coastal regions.

3.4 Open ocean biomes

The analysis in this section will address changes in nutrient concentration and biological productivity by ocean biome. Following Sarmiento et al. (2004), we use average vertical velocity, maximum wintertime mixed layer depth and sea ice cover to define six biomes that are differentiated based on physical circulation features. They are: (1) equatorially influenced, between 5° S and 5° N, divided into upwelling and downwelling regions, (2) marginal sea ice zones that are covered by sea ice at least once during the year, (3) permanently stratified subtropical biomes where downwelling occurs and maximum mixed layer depth is ≤ 150 m, (4) seasonally stratified subtropical biomes where downwelling occurs and maximum mixed layer depth >150 m, (5) low-latitude upwelling regions between 35° S and 30° N, and (6) all subpolar upwelling regions north of 30° N

BGD
12, 3905–3942, 2015

and south of 25° S. Boundaries were determined based on circulation features from the respective model runs for consistency.

The largest changes in biome areal extent include a 19 % increase in the Northern Hemisphere marginal ice zone and −9 % change in the extent of the neighboring subpolar Northern Hemisphere biome, as shown in table 1. Differences in surface chlorophyll, biomass and macronutrients between the two model runs (see table 2) show the addition of CDM results in several important qualitative and regionally specific changes. For example, the greatest relative change in chlorophyll and biomass over the upper 10 m are found in equatorial and low latitude biomes, with 15–17 % increases in biomass and 21–24 % increases in chlorophyll. Meanwhile, the greatest changes in depth-integrated chlorophyll and biomass are found in high latitude regions. In the Northern Hemisphere subpolar biome, chlorophyll decreased by 14 % and biomass decreased by 15 %. Chlorophyll and biomass decreased by 9 and 10 % in the Southern Hemisphere marginal ice zone. The following analysis seeks to understand this mismatch between surface and subsurface trends between biomes. In particular, why are the largest changes in surface chlorophyll near the equator and largest changes in depth-integrated chlorophyll at higher latitudes?

As shown in previous sections, phytoplankton move up in the water column when CDM is included. The resulting vertical profile of chlorophyll is altered in different ways depending on the biome. To illustrate, we choose three representative biomes from various latitudes, for which chlorophyll profiles are shown in Fig. 11. In the equatorial upwelling and seasonally stratified biomes, the deep chlorophyll maximum is increased. In the ice NH region, where light delivery is seasonally dependent, chlorophyll is found in highest concentrations near the surface and is diminished at depth. In every biome, there is more chlorophyll near the surface but less chlorophyll beyond some depth. These changes can be attributed to a combination of diminished light availability and increased nutrient availability.

Globally averaged profiles of the relative difference in irradiance and macronutrient concentration are shown in Fig. 12. Over the upper 200 m, there are more nutrients

BGD
12, 3905–3942, 2015

and less irradiance at all depths. Referring back to Fig. 7a, there is more biomass near the surface, but diminished biomass at depth. These plots show that as we move down the water column, there is a changing balance of nutrient and light availability affecting phytoplankton growth. The increased abundance of nutrients fuels the growth of phytoplankton near the surface. At depth, light limitation is increased to a level that results in diminished phytoplankton productivity.

We analyze the competition of light and nutrient availability on biomass using the light and nutrient limitation factors previously discussed in the Methodology section. The average light and nutrient limitation scaling factors over the surface 10 m of each open ocean biome and the coastal region for the chl-only run are shown in Fig. 13a. Consider the placement of the various biomes on this plot for the model run where light attenuation depends on chlorophyll alone. The equatorial regions are least light limited, so they lie to the right on the x axis. The marginal ice zones and subpolar regions are most light limited and lie to the left on the x axis. The Southern Hemisphere biomes are in general more nutrient limited than their Northern Hemisphere counterparts, due to modeled iron limitation. They are found lower on the y axis.

As additional light limitation is introduced by the inclusion of light absorption by CDM in the k_d parameterization, these markers shift. Panel b of Fig. 13 shows nlim and llim averaged over the surface 10 m for the chl&CDM model run. The displacement of these points from panel a to its new coordinates in panel b are shown in vector form in panel c. The vector begins at its coordinates from panel a, i.e. values from the chl-only run, and terminates with an "x" at the new coordinates from the chl&CDM model run. This vector indicates the change in nutrient and light limitation between the two model experiments.

The impact of these changes in light and nutrients on biomass can be seen by overlaying lines of constant biomass on these plots. Using Eq. (10), we utilize the fact that in the BLING model, biomass scales as $(C(\text{nlim} \times \text{llim})^3 + (\text{nlim} \times \text{llim}))$. In panel c, all biome vectors are pointed in the left and upward direction, indicating more nutrient availability and less light availability. The vectors cross contours of constant biomass in the direc-

BGD
12, 3905–3942, 2015

tion of increasing biomass. Additional nutrient availability fuels increases in biomass in the upper 10 m of the ocean in almost every ocean biome, which is in agreement with the results reported in table 2. Panel d is similar to panel c, but with nlim, llim values averaged over the upper 200 m of the ocean. Here, the vectors are moving in a direction that crosses lines of decreasing biomass. This is consistent with results shown in table 3. In this case, the decrease in light availability drives the decrease in biomass, despite the increase in nutrients.

The two clusters of vectors, i.e. nlim and llim averaged over (1) 0 to 10 m constituting a "euphotic regime" and (2) 0 to 200 m constituting a "subsurface regime", are shown on the same plot for comparison in Fig. 14. To first order, we think of the euphotic regime as the depth range that dominates the signal seen by satellite observations and the subsurface regime as the integrated impact over the entire ecosystem. The key difference between the two regimes is the vectors in the surface regime are crossing lines of constant biomass in the increasing biomass direction, while the vectors in the subsurface regime are crossing lines of constant biomass in the decreasing biomass direction. While there is a noticeable difference in the magnitude and angle of the vectors between these two regimes, these differences are only meaningful in the context of the vector's placement in the domain. For example, the greatest decreases in depth-integrated biomass from the inclusion of CDM were found in high latitude biomes and coastal region. This is most pronounced in the costal region, where biomass diminished by 18 %. The corresponding magenta vector in this plot noticeably spans the greatest distance in the direction of decreasing biomass contour lines. Although the vector for the Northern Hemisphere marginal ice zone ("ice nh") is smaller, it is placed in the upper left hand corner where the contour lines are closer together. It crosses the appropriate number of lines of constant biomass to indicate the 10 % drop in biomass in this region when CDM is included. In the surface regime, the greatest increases in biomass are in the equatorial biomes. The "eq up" and "eq down" vectors are short, shown in Fig. 13c, the slope of the vector indicates sufficient positive displacement in the y direction which allows for increasing biomass. The slope of some of the higher

BGD
12, 3905–3942, 2015

latitude vectors, such as the seasonal stratified biomes are more parallel to the lines of constant biomass, which accounts for the smaller changes in surface biomass.

Increases in surface chlorophyll ranged from 15 to 24 % in the equatorial, low-latitude and permanently stratified biomes. In these areas, depth-integrated biomass decreased by ≤ 6 %. These biomes comprise the cluster of vectors on the bottom right hand side of the plot in Fig. 14. The variation in surface chlorophyll appears to depend on the seasonal availability of light, since the biomes are similarly nutrient limited. In these biomes, shoaling the euphotic zone concentrates phytoplankton closer to the surface. In equatorial and low-latitude regions, the steady supply of light and upwelling currents keep phytoplankton near the surface mostly year-round. Here, surface chlorophyll increased by 21 to 24 %. In the permanently stratified biome, there are intermittent mixing events and, on average, downwelling currents. Mixing the phytoplankton throughout the water column has the effect of reducing the concentration of phytoplankton near the surface. Any increases in surface chlorophyll in the stratified regions will be intermittent and by annual average smaller than the changes found near the equator, which explains why surface chlorophyll increased by 15 % in the permanently stratified biome.

4 Conclusions

This paper addressed the impact of colored detrital matter on biological production by altering the visible light field in the GFDL CM2Mc Earth System Model with BLING biogeochemistry. Light absorption by detrital matter and CDOM, a_{dg}, was prescribed using a satellite dataset with near-complete global surface ocean coverage. Results show that increasing light limitation can decouple surface trends in modeled biomass and macronutrients. Although increased biomass is usually associated with high productivity and decreased nutrients, this was not the case in our light-limited model runs. Surface chlorophyll, biomass and nutrients all increased together. These changes can be attributed to the movement of biological productivity higher up the water column,

BGD
12, 3905–3942, 2015

which increases surface chlorophyll and biomass while simultaneously decreasing depth-integrated biomass. Meanwhile, diminished total biomass leaves excess nutrients in the water column that are eventually delivered to the surface, elevating surface macronutrient concentrations. While absolute changes in chlorophyll and macronutrient concentrations were small, one key qualitative outcome of this model experiment is that surface biomass trends may not reflect how light limitation is reducing ecosystem productivity. Understanding changes in ecosystem productivity requires both surface and depth-resolved information.

Adding the optical impact of CDM decreased integrated coastal biomass and chlorophyll concentration by 18 %. Meanwhile, surface chlorophyll concentration in coastal regions increased by 35 %. The open ocean biome analysis showed how, in the BLING model, changes in surface chlorophyll and biomass over the upper 200 m in various biomes depend on a combination of light and nutrient availability. In the high latitudes, adding CDM to the light-only limited Northern Hemisphere vs. the iron-light colimited Southern Hemisphere seemed to have different impacts on biomass decline. In the low- to mid-latitudes, the circulation patterns and its impact on light availability determines the structure of the chlorophyll profile and the response of that biome to a shrinking euphotic zone. These results highlight the biomes that may be most vulnerable to changes in biomass and chlorophyll if met with changes in light availability. For example high-latitude biomes that were already light limited experienced the greatest drop in biomass from additional light limitation.

In this study, the spatial distribution of a_{dg} was fixed, so it could not respond to changes in the light field as chlorophyll concentration is able to do in the CM2Mc-BLING coupled physical-biogeochemical model configuration. The a_{dg} values were constant with time so the seasonal cycle was not represented. Analysis of satellite monthly climatology data shows there is more variability near river mouths and equatorial upwelling zones. Furthermore, surface values were held constant throughout the water column. Resolving these simplifications may have important impacts. An interactive CDOM tracer would be best suited for such a task, once the mechanisms that con-

BGD
12, 3905–3942, 2015

trol the production and degradation of CDM are better understood. Previous work has elucidated some potential sources and sinks of CDOM to the ocean, including in situ production by heterotrophic microbial activity (Nelson et al., 2004), delivery by freshwater input from terrestrial sources and degradation by photobleaching when exposed to intense light conditions (Blough and DelVecchio, 2002). Recently, Nelson et al. (2010) showed the depth-resolved cross-sections of a_{CDOM} through the major ocean basins approximately follow apparent oxygen utilization contours. This suggests that oxygen might be used to improve modeling depth-dependent CDOM distributions in the future. Direct modeling of CDOM would be of particular importance to regions where CDOM abundance is in flux due to changes in the volume and composition freshwater runoff. In the Arctic Ocean, CDOM is of primary importance in determining the non-water absorption coefficient of light and its relatively concentrated presence increases energy absorbed in the mixed layer by trapping incoming shortwave radiation (Pegau, 2002). Hill (2008) used a radiative transfer model to find the absorption of shortwave radiation by CDOM can increase energy absorbed by the mixed layer by 40 % over pure seawater and this additional energy can account for 48 % of springtime ice melt by water column heating. These impacts should be incorporated into future earth system models and existing higher resolution regional models to more accurately simulate the ocean heat budget and marine biogeochemistry.

Acknowledgements. This work was supported by NASA Headquarters under the NASA Earth and Space Science Fellowship Program – Grant NNX14AK98H.

References

Blough, N. V. and DelVecchio, R.: Chapter 10: Chromophoric DOM in the Coastal Environment, in: Biogeochemistry of Marine Dissolved Organic Matter, edited by: Hansell, D. A., and Carlson, C. A., Academic Press, San Diego, 509–546, doi:10.1016/B978-012323841-2/50012-9, 2002. 3923

BGD
12, 3905–3942, 2015

Dunne, J. P., Armstrong, R. A., Gnanadesikan, A., and Sarmiento, J. L.: Empirical and mechanistic models for the particle export ratio, Global Biogeochem. Cy., 19, GB4026, doi:10.1029/2004GB002390, 2005. 3913

Eppley, R.: Temperature and phytoplankton growth in the sea, Fishery Bulletin, 70, 1063–1085, 1972. 3912

Galbraith, E. D., Gnanadesikan, A., Dunne, J. P., and Hiscock, M. R.: Regional impacts of iron-light colimitation in a global biogeochemical model, Biogeosciences, 7, 1043–1064, doi:10.5194/bg-7-1043-2010, 2010. 3910, 3912, 3914

Galbraith, E. D., Kwon, E. Y., Gnanadesikan, A., Rodgers, K. B., Griffies, S. M., Bianchi, D., Sarmiento, J. L., Dunne, J. P., Simeon, J., Slater, R. D., Wittenberg, A. T., and Held, I. M.: Climate Variability and Radiocarbon in the CM2Mc Earth System Model., J. Climate, 24, 4230–4254, 2011. 3910, 3912

Garcia, H. E., Locarnini, R. A., Boyer, T. P., Antonov, J. I., Baranova, O., Zweng, M., Reagan, J., and Johnson, D.: World Ocean Atlas 2013, Volume 4: Dissolved Inorganic Nutrients (phosphate, nitrate, silicate), NOAA Atlas NESDIS 76, edited by: Levitus, S. and Mishonov, A., 2014. 3932

Gnanadesikan, A. and Anderson, W. G.: Ocean water clarity and the ocean general circulation in a coupled climate model., J. Phys. Oceanogr., 39, 314–332, 2009. 3908

Gregg, W. W. and Casey, N. W.: Skill assessment of a spectral ocean–atmosphere radiative model, J. Marine Syst., 76, 49–63, doi:10.1016/j.jmarsys.2008.05.007, 2009. 3910

Hill, V. J.: Impacts of chromophoric dissolved organic material on surface ocean heating in the Chukchi Sea, J. Geophys. Res.-Oceans, 113, C07024, doi:10.1029/2007JC004119, 2008. 3923

Manizza, M., Le Quéré, C., Watson, A. J., and Buitenhuis, E. T.: Bio-optical feedbacks among phytoplankton, upper ocean physics and sea-ice in a global model, Geophys. Res. Lett., 32, L05603, doi:10.1029/2004GL020778, 2005. 3908, 3910, 3914

Morel, A.: Optical modeling of the upper ocean in relation to its biogenous matter content (case I waters), J. Geophys. Res.-Oceans, 93, 10749–10768, doi:10.1029/JC093iC09p10749, 1988. 3907

Murtugudde, R., Beauchamp, J., McClain, C. R., Lewis, M., and Busalacchi, A. J.: Effects of penetrative radiation on the upper tropical ocean circulation., J. Climate, 15, 470–486, 2002. 3908

BGD
12, 3905–3942, 2015

Nelson, N. B. and Siegel, D. A.: The global distribution and dynamics of chromophoric dissolved organic matter, Annual Review of Marine Science, 5, 447–476, doi:10.1146/annurev-marine-120710-100751, pMID: 22809178, 2013. 3909, 3911

Nelson, N. B., Carlson, C. A., and Steinberg, D. K.: Production of chromophoric dissolved organic matter by Sargasso Sea microbes, Mar. Chem., 89, 273–287, doi:10.1016/j.marchem.2004.02.017, 2004. 3923

Nelson, N. B., Siegel, D. A., Carlson, C. A., and Swan, C. M.: Tracing global biogeochemical cycles and meridional overturning circulation using chromophoric dissolved organic matter, Geophys. Res. Lett., 37, L03610, doi:10.1029/2009GL042325, 2010. 3923

Ohlmann, J. C. and Siegel, D. A.: Ocean radiant heating. Part II: Parameterizing solar radiation transmission through the upper ocean, J. Phys. Oceanogr., 30, 1849–1865, doi:10.1175/1520-0485(2000)030<1849:ORHPIP>2.0.CO;2, 2000. 3907

Pegau, W. S.: Inherent optical properties of the central Arctic surface waters, J. Geophys. Res.-Oceans, 107, SHE 16-1–SHE 16-7, doi:10.1029/2000JC000382, 2002. 3923

Sarmiento, J. L. and Gruber, N.: Ocean Biogeochemical Dynamics, Princeton University Press, Princeton, New Jersey, 2006. 3916

Sarmiento, J. L., Slater, R., Barber, R., Bopp, L., Doney, S. C., Hirst, A. C., Kleypas, J., Matear, R., Mikolajewicz, U., Monfray, P., Soldatov, V., Spall, S. A., and Stouffer, R.: Response of ocean ecosystems to climate warming, Global Biogeochem. Cy., 18, GB3003, doi:10.1029/2003GB002134, 2004. 3917, 3937

Siegel, D. A., Maritorena, S., Nelson, N. B., and Behrenfeld, M. J.: Independence and interdependencies among global ocean color properties: reassessing the bio-optical assumption, J. Geophys. Res.-Oceans, 110, C07011, doi:10.1029/2004JC002527, 2005. 3909

Werdell, P. J. and Bailey, S. W.: An improved in-situ bio-optical data set for ocean color algorithm development and satellite data product validation, Remote Sens. Environ., 98, 122–140, doi:10.1016/j.rse.2005.07.001, 2005. 3911

Yoder, J. A. and Kennelly, M. A.: Seasonal and ENSO variability in global ocean phytoplankton chlorophyll derived from 4 years of SeaWiFS measurements, Global Biogeochem. Cy., 17, 23-1–23-14, doi:10.1029/2002GB001942, 2003. 3931

BGD
12, 3905–3942, 2015

Table 1. Surface area by biome, in km^2 with percentage change in area between the two model runs (chl&CDM minus chl-only).

Biome	chl&CDM	% age of total	chl-only	% age of total	% change
Equatorial Upwell	1.86×10^7	6 %	1.86×10^7	6 %	0 %
Equatorial Downwell	8.34×10^6	3 %	8.07×10^6	3 %	3 %
Low Latitude Upwell	6.32×10^7	21 %	6.32×10^7	21 %	0 %
Permanently Stratified	1.01×10^8	34 %	9.89×10^7	33 %	2 %
Seasonally Stratified	3.93×10^7	13 %	4.11×10^7	14 %	−4 %
Subpolar NH	1.22×10^7	4 %	1.35×10^7	4 %	−9 %
Ice NH	1.17×10^7	4 %	9.81×10^6	3 %	19 %
Subpolar SH	2.33×10^7	8 %	2.43×10^7	8 %	−4 %
Ice SH	2.37×10^7	8 %	2.27×10^7	8 %	4 %

BGD
12, 3905–3942, 2015

Table 2. Difference in surface chlorophyll mg m^{-3}, biomass mg C m^{-3} and macronutrient μM concentrations, chl&CDM minus chl-only. Surface values are the average over the top 10 m. All surface changes are statistically significant to three SDs. Statistical significance tests were performed on decadally smoothed data from the the final 100 years of the two model runs.

Biome	Δ chl	% Δ	Δ biomass	% Δ	Δ nutrient	% Δ
Equatorial Upwell	0.28	22 %	4.5	16 %	0.053	14 %
Equatorial Downwell	0.23	24 %	4.2	17 %	0.052	24 %
Low Latitude Upwell	0.21	21 %	3.1	15 %	0.038	20 %
Permanently Stratified	0.18	15 %	2.0	10 %	0.036	13 %
Seasonally Stratified	0.52	7 %	2.2	5 %	0.066	15 %
Subpolar NH	0.83	9 %	4.2	7 %	0.071	19 %
Ice NH	0.90	18 %	7.7	14 %	0.10	23 %
Subpolar SH	0.29	7 %	0.97	3 %	0.041	3 %
Ice SH	0.18	11 %	1.3	6 %	0.038	2 %

BGD
12, 3905–3942, 2015

Table 3. Difference in chlorophyll mg m^{-2}, biomass mg C m^{-2} and macronutrients mmol m^{-2} between the two model runs (chl&CDM minus chl-only), integrated over the upper 200 m.

Biome	Δ chl	% Δ	Δ biomass	% Δ	Δ nutrient	% Δ
Equatorial Upwell	−1.7	−7 %	−87	−6 %	15	8 %
Equatorial Downwell	−1.2	−5 %	−67	−5 %	17	11 %
Low Latitude Upwell	−0.74	−4 %	−38	−3 %	13	9 %
Permanently Stratified	−0.77	−4 %	−61	−4 %	11	11 %
Seasonally Stratified	−2.2	−5 %	−127	−5 %	16	13 %
Subpolar NH	−8.8	−14 %	−482	−15 %	15	11 %
Ice NH	−2.2	−5 %	−179	−8 %	22	16 %
Subpolar SH	−1.6	−5 %	−139	−6 %	7.4	2 %
Ice SH	−2.1	−9 %	−165	−10 %	5.3	1 %

BGD
12, 3905–3942, 2015

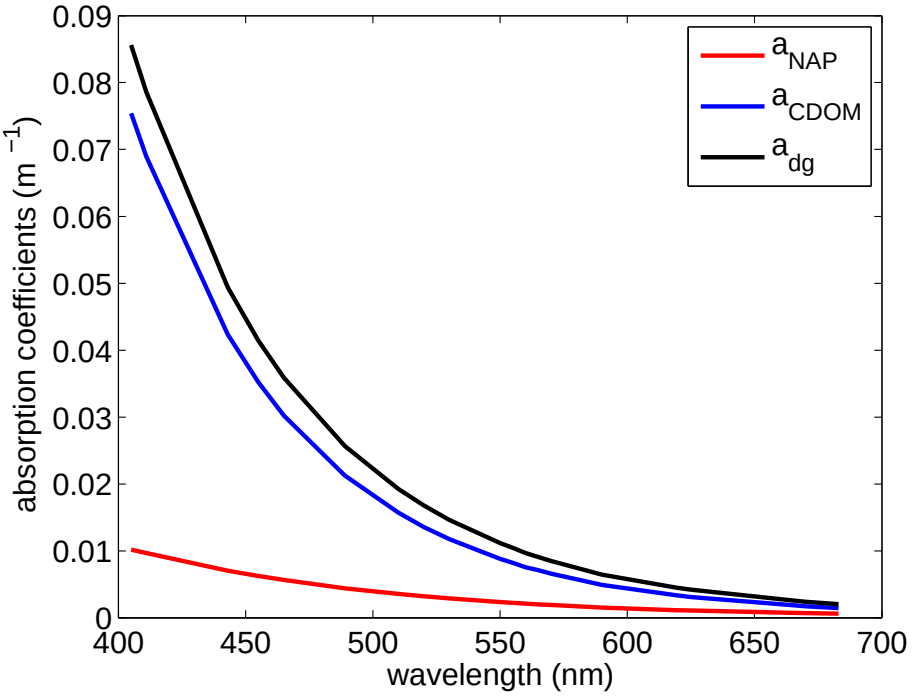

Figure 1. Median IOP spectra from NOMAD dataset. In the visible spectrum, CDOM absorption is strongest in the blue and decreases exponentially with increasing wavelength.

BGD
12, 3905–3942, 2015

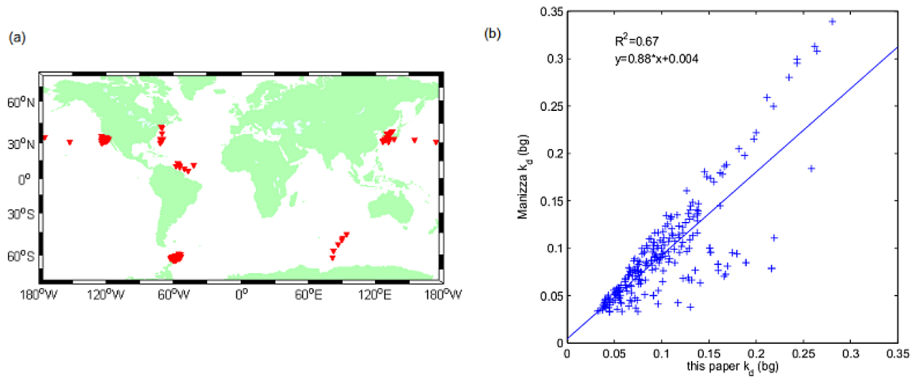

Figure 2. (a) Map of stations with locations of the 244 in-situ measurements used to develop the k_d(bg) parameterization with CDM, Eq. (5) **(b)** comparison of Eqs. (3) and (5) applied to NOMAD in situ chlorophyll concentration and a_{dg}(443) measurements to calculate k_d(bg). The 0.88 slope on the regression line indicates that when CDM is included, k_d(bg) increases more rapidly than when it depends on chlorophyll concentration alone.

BGD
12, 3905–3942, 2015

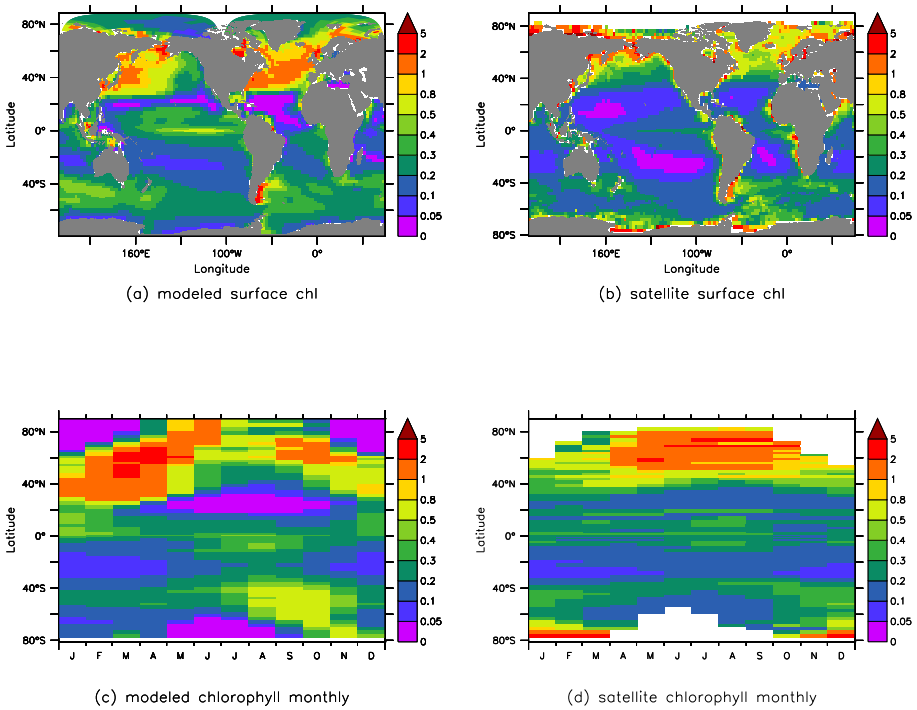

Figure 3. Comparison of **(b, d)** chlorophyll concentration in mg m^{-3} from SeaWiFS satellite observation (Yoder and Kennelly, 2003) used in earlier similar studies and **(a, c)** modeled using GFDL ESM CM2Mc with BLING biogeochemistry. Data shown are from the chl&CDM model run described in Sect. 4 of this paper. Annual average surface distributions are shown in **(a, b)** and monthly average surface concentration by latitude are shown in **(c, d)**.

BGD
12, 3905–3942, 2015

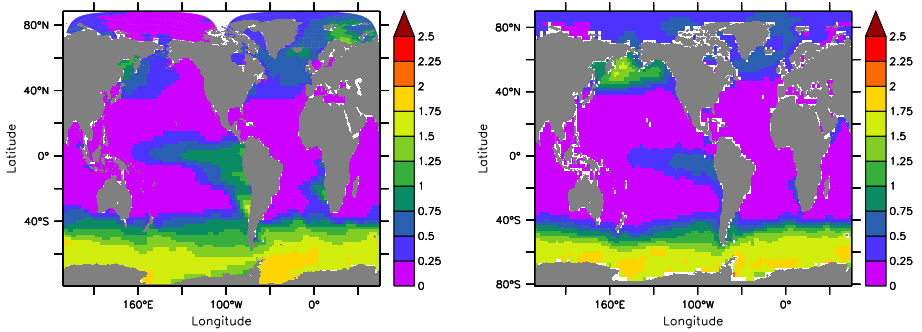

Figure 4. Comparison of **(a)** modeled using GFDL CM2Mc with BLING biogeochemistry and **(b)** measured macronutrient concentration, $\frac{1}{2}(PO_4 + \frac{NO_3}{16})$, from World Ocean Atlas 2013 nitrate and phosphate datasets. Concentration in μM (Garcia et al., 2014).

BGD
12, 3905–3942, 2015

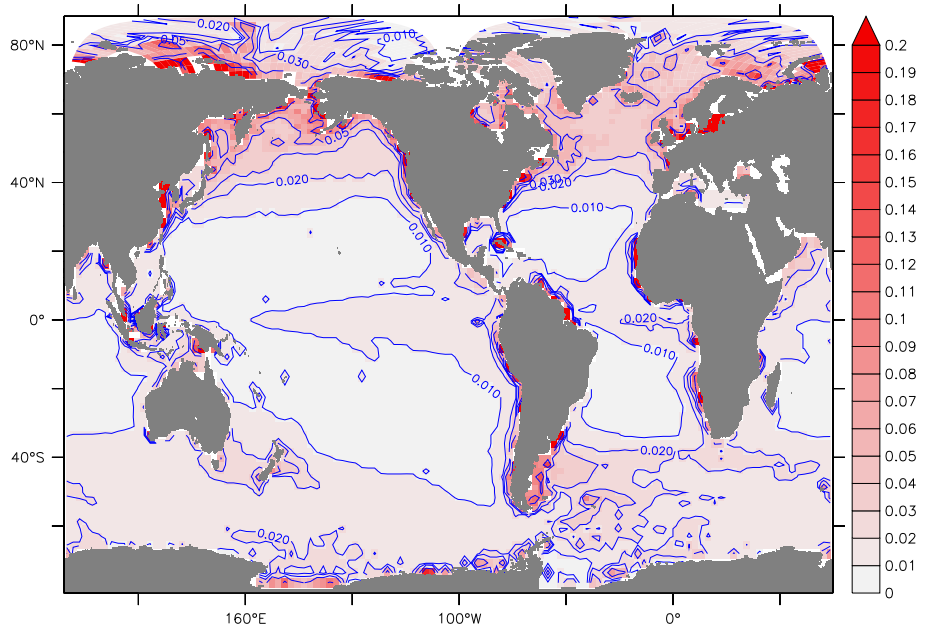

Figure 5. The spatial distribution of $a_{dg}(443)$ as prescribed in the model runs for this paper, mapped onto the CM2Mc ESM tracer grid with data extrapolated into polar regions.

BGD
12, 3905–3942, 2015

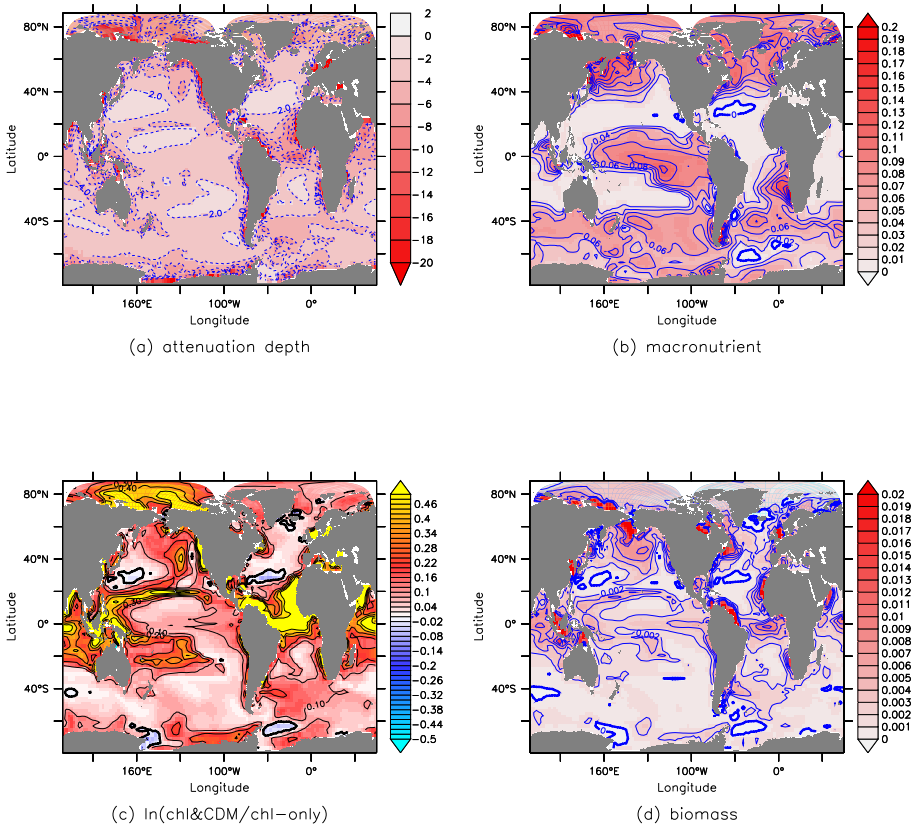

Figure 6. Difference **(a)** attenuation depth m, **(b)** surface macronutrient concentration μM, **(c)** surface chlorophyll concentration and **(d)** surface biomass concentration $g\,C\,m^{-3}$; chl&CDM minus chl-only. Surface values represent the average over the top 10 m. Panel **(c)** shows natural log ratio of chlorophyll concentration from the chl&CDM run over chl-only run, so positive values indicate an increase in chlorophyll in the chl&CDM run.

BGD
12, 3905–3942, 2015

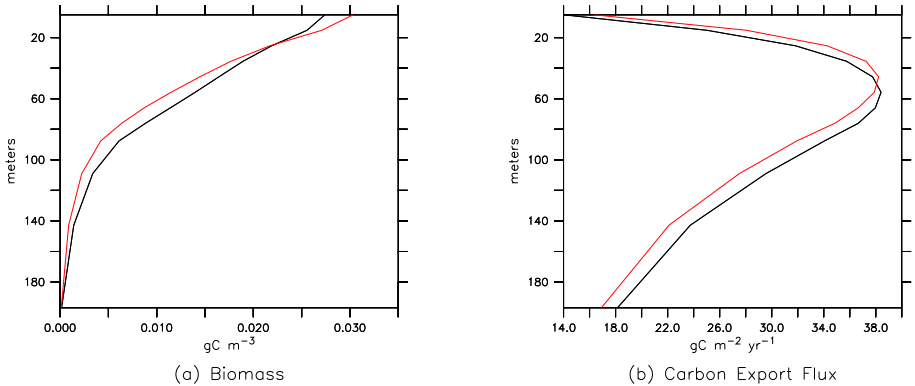

Figure 7. Globally averaged profile of **(a)** biomass in g C m^{-3} and **(b)** carbon export flux in g C m^{-2} yr^{-1}. Black line shows data from the chl-only run, red line represents chl&CDM run.

BGD
12, 3905–3942, 2015

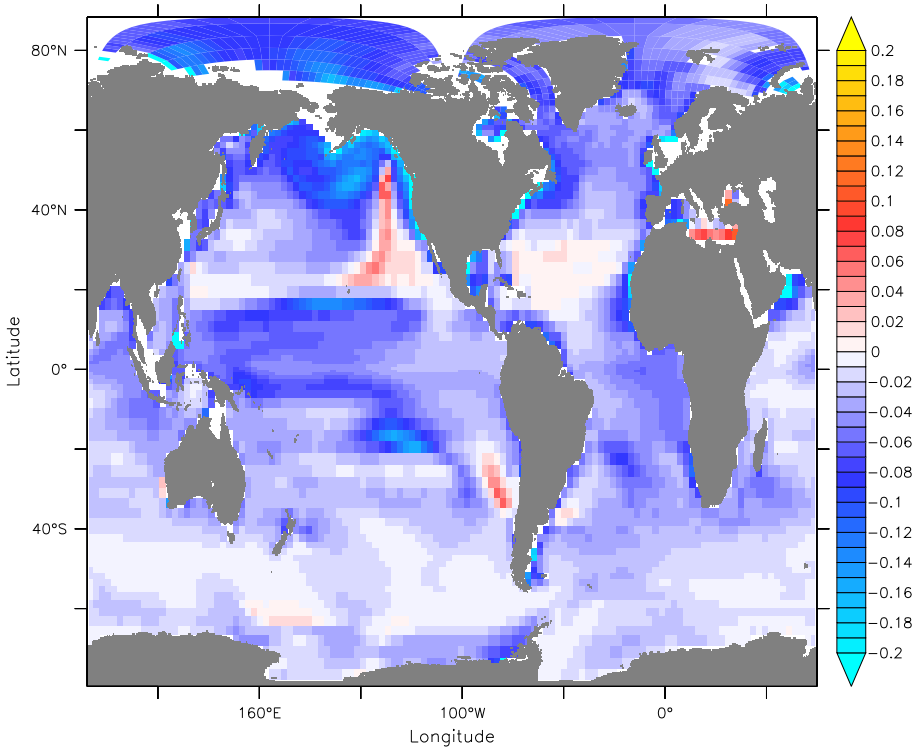

Figure 8. Difference in E_{bp}, chl&CDM model run minus chl-only model run.

BGD
12, 3905–3942, 2015

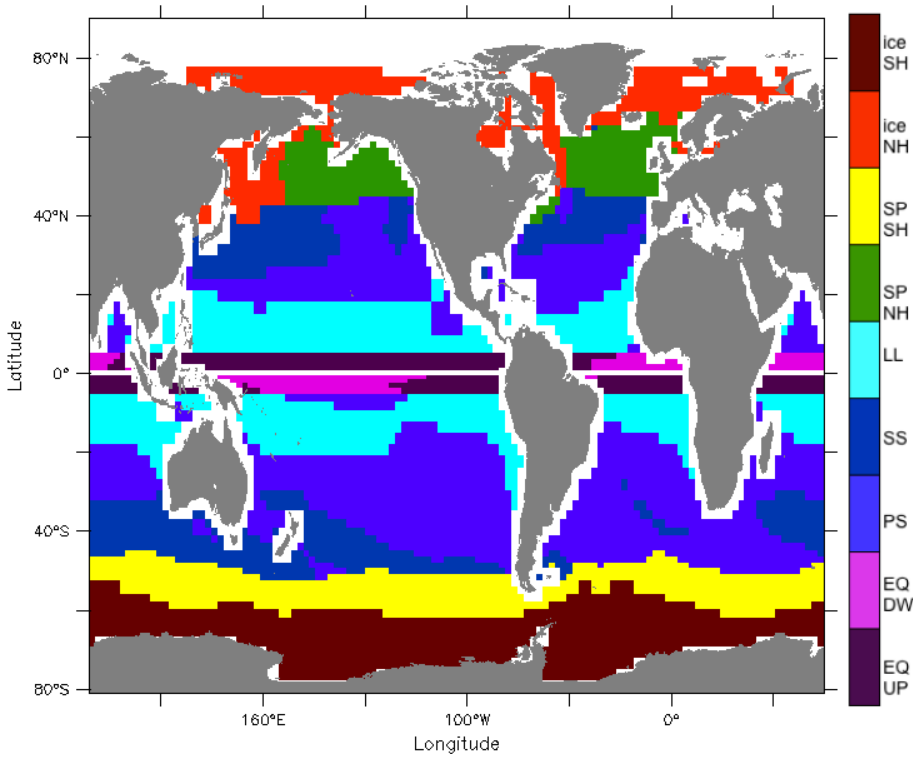

Figure 9. Biomes as defined by Sarmiento et al. (2004) applied to GFDL CM2Mc with chl&CDM k_d parameterization, Eq. (5). Legend abbreviations: ice = marginal ice zone, SP = subpolar, LL = lower latitude, SS = seasonally stratified, PS = permanently stratified, EQ DW = equatorial downwelling, EQ UP = equatorial upwelling. Suffixes NH and SH stand for northern hemisphere and southern hemisphere.

BGD
12, 3905–3942, 2015

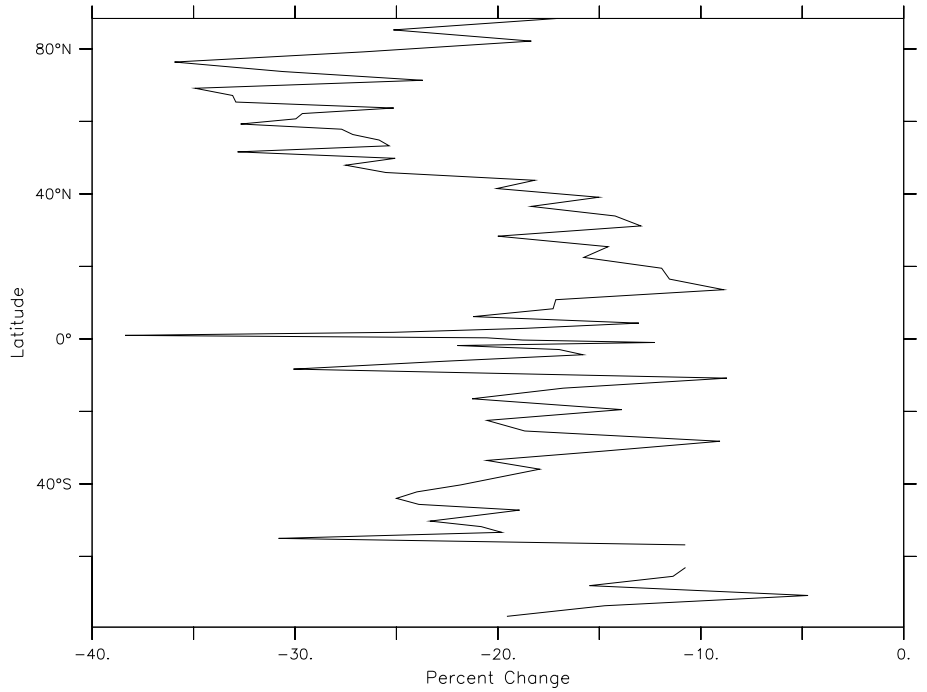

Figure 10. Percent change in total integrated biomass in coastal regions, by latitude. Coastal regions are defined as model grid boxes adjacent to land.

BGD
12, 3905–3942, 2015

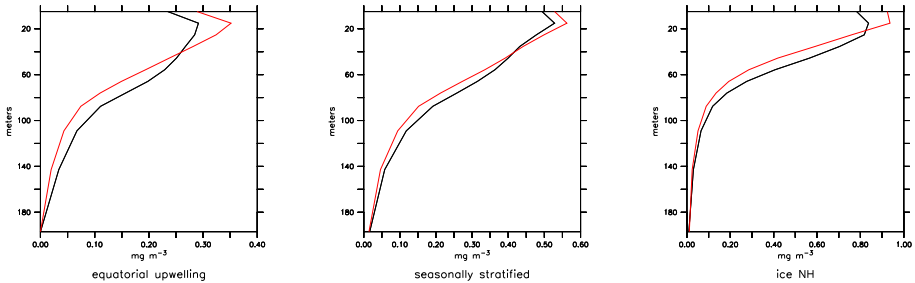

Figure 11. The depth profile of chlorophyll concentration mg m^{-3} in three biomes. The black line indicates the chl-only run, red line represents chl&CDM run. The equatorial upwelling and seasonally stratified biomes show increased peaks in the deep chlorophyll maximum (DCM) when CDM is included. All three biomes show increased chlorophyll near the surface, but diminished chlorophyll at depth.

BGD
12, 3905–3942, 2015

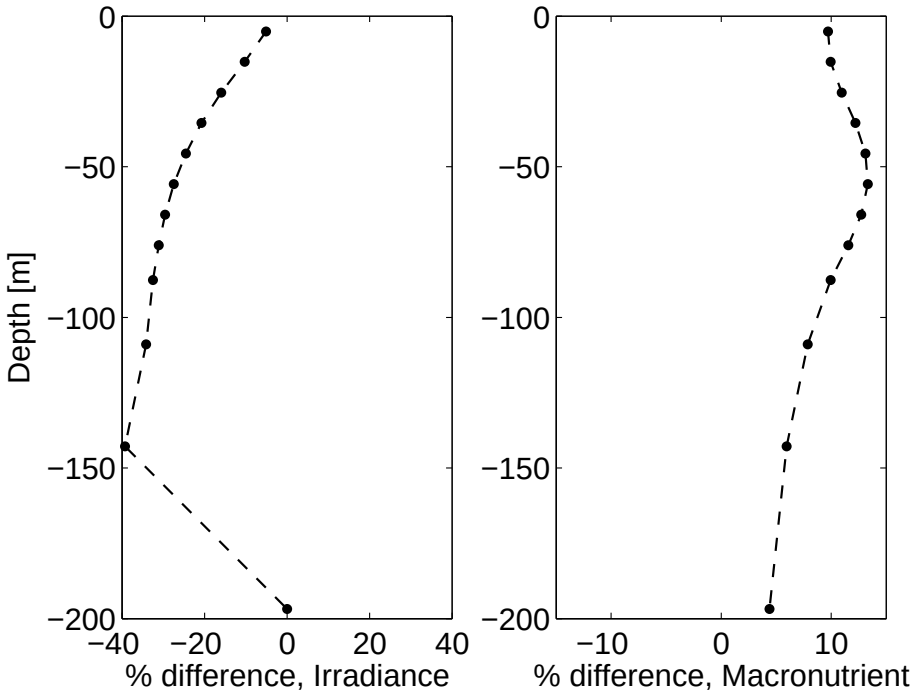

Figure 12. Profiles of percent change in globally averaged irradiance and macronutrient concentration, chl-only minus chl&CDM. There is a decrease in irradiance and increase in macronutrients throughout the upper 200 m. The percentage difference in irradiance is 0 at 200 m because 200 m is the model-prescribed maximum light penetration depth.

BGD
12, 3905–3942, 2015

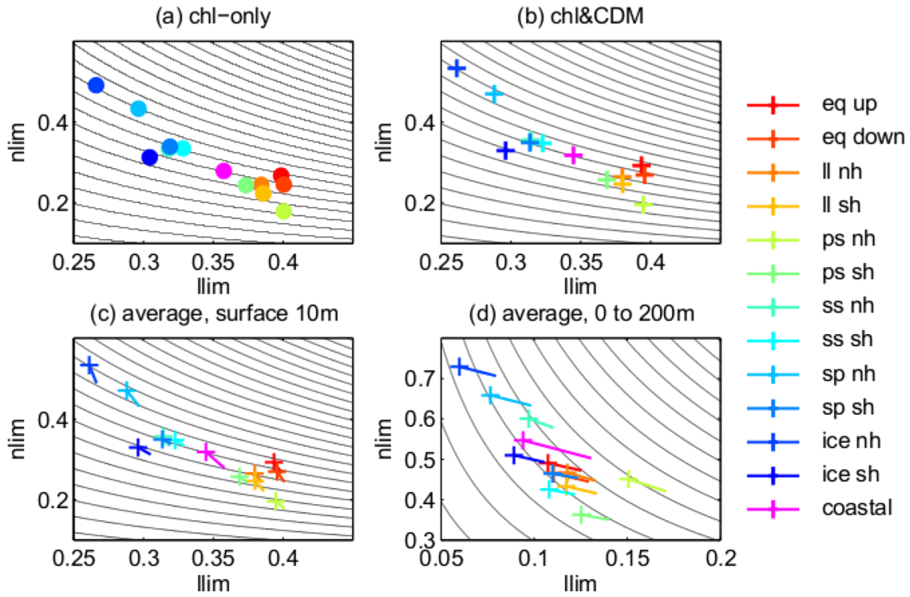

Figure 13. Light and nutrient limitation scaling factors for open ocean biomes and coastal regions. **(a)** Average nlim, llim for chl-only model run, from 0 to 10 m **(b)** average nlim, llim for chl&CDM model run, from 0 to 10 m **(c)** vectors connecting coordinates from panel **(a, b)**, average from 0 to 10 m. **(d)** Vectors starting at coordinates from chl-only model run and terminating with an "*x*" at values from chl&CDM model run, average from 0 to 200 m. Legend abbreviations: ice = marginal ice zone, sp = subpolar, ss = seasonally stratified, ps = permanently stratified, ll = lower latitude, equp = equatorial upwelling, eqdown = equatorial downwelling, coastal = coastal regions, defined as the grid cells adjacent to land. Suffixes nh and sh stand for Northern Hemisphere and Southern Hemisphere.

BGD
12, 3905–3942, 2015

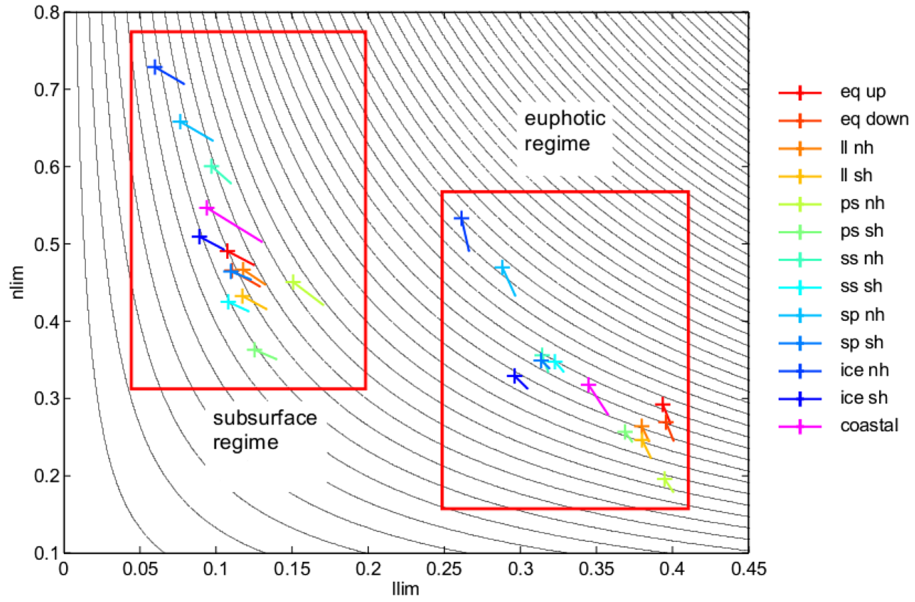

Figure 14. All vectors from Fig. 13c and d, on the same plot. Vectors for nlim, llim values averaged over the upper 10 m occupy the "euphotic regime" and values averaged over the upper 200 m occupy the "subsurface regime".

BGD
12, 3905–3942, 2015